Research Article

Highly fluorescent CsPbBr$_3$/TiO$_2$ core/shell perovskite nanocrystals with excellent stability

Haitao Chen[1,2,3] · Renhua Li[1,3] · Anqi Guo[1,3] · Yu Xia[1,3]

© The Author(s) 2021   OPEN

Abstract

The poor stability of CsPbX$_3$ (X = Cl, Br, I) perovskite nanocrystals is the most impediment to its application in the field of photoelectrics. In this work, monodisperse CsPbBr$_3$/TiO$_2$ nanocrystals are successfully prepared by coating titanium precursor on the surface of colloidal CsPbBr$_3$ nanocrystals at room temperature. The CsPbBr$_3$/TiO$_2$ nanocomposites exhibit excellent stability, remaining the identical particle size (9.2 nm), crystal structures and optical properties. Time-resolved photoluminescence decay shows that the lifetime of CsPbBr$_3$/TiO$_2$ nanocrystals is about 4.04 ns and keeps great stability after lasting two months in the air. Results show that the coating of TiO$_2$ on CsPbBr$_3$ NCs greatly suppressed the anion exchange and photodegradation, which are the main reasons for dramatically improving their chemical stability and photostability. The results provide an effective method to solve the stability problem of perovskite nanostructures and are expected to have a promising application in optoelectronic fields

Article highlights

1. Prepared the all-inorganic CsPbBr$_3$/TiO$_2$ core/shell perovskite nanocrystals by an easy method.
2. Explored its essences of PL and lifetime of the synthesized CsPbBr$_3$/TiO$_2$ perovskite nanocrystals.
3. CsPbBr$_3$/TiO$_2$ nanocrystals show the great thermal stability after the post-annealing.
4. The CsPbBr$_3$/TiO$_2$ nanocrystals have a high PLQY and have a promising application in solar cells.

1 Introduction

Owing to the high absorption coefficient, long carrier diffusion distance, tunable emission bandgap and high photoluminescence quantum yield, colloidal metal halide perovskite nanocrystals have been intensively explored in laser, photodetector, light-emitting diode (LED) and solar cell [1–4]. Kojima et al. [5] prepared the earliest perovskite solar cells, selecting organic–inorganic hybrid perovskite materials CH$_3$NH$_3$PbX$_3$ (X = Br, I) as new photosensitizer to

---

✉ Haitao Chen, htchen@yzu.edu.cn | [1]College of Physics Science and Technology, Yangzhou University, Yangzhou 225002, People's Republic of China. [2]National Laboratory of Solid State Microstructures, Laboratory of Modern Acoustics of MOE, Nanjing University, Nanjing 210093, People's Republic of China. [3]China Resources Microelectronics Co., Ltd, No. 14 Liangxi Road, Wuxi City 214061, People's Republic of China.

replace the dyes in traditional DSSCs. However, due to the large bandgap, the photoelectric conversion efficiency is only about 3.8%, which extremely obstructs their prelude as the light-absorbing material.

Recently, due to particular crystal structure, high energy conversion rate, low cost and mild conditions, organic–inorganic hybrid perovskite nanostructure have attracted much attention of the academic and industry community [6, 7]. Under ongoing efforts, the photoelectric conversion efficiency has rapidly increased to 22.1% [8]. Liu et al. [9] added iodide ions to the organic cation solution and realized the high-efficiency PSC film based on "lead halide perovskite" absorbent and achieved the 22.1% energy efficiency in small batteries. In 2018, École Polytechnique Fédérale de Lausanne (EPFL) refreshed the world efficiency record of CIGS perovskite solar cells to 23.3% [10]. Similarly, Chen et al. [11] designed an inorganic perovskite device by adjusting bandgap at different positions, which increased the film thickness and reduced the charge recombination, behaving 15.2% of the final photoelectric conversion efficiency. Recently, the groundbreaking cell produced by Oxford PV has been proven to convert 29.52% of solar energy into electricity. However, when exposed to moisture, humidity, glare and high temperature, the perovskite nanocrystals would decompose and decrease their environmental stability. These uncontrollable factors block the development of nanocrystals in practical applications [12, 13].

Recently, significant efforts have been committed to increasing the stability of perovskite nanocrystals, by embedding a protective semiconductor matrix, adulterating photocurable fluoropolymer or compounding to molecular sieve material with regular porous structure [14]. Employing a facile solution-phase method, Zhou et al. prepared $CsPbX_3$/ZnS nanocrystal heterodimer with a high quality and enhanced stability, which offers an interesting playground to design and fabricate novel perovskite heterostructures [15]. Zhang et al. [16] successfully prepared high-stability $CsPbX_3$/SiO_2 Janus nanoparticles, and the photoluminescence quantum yield reached 80%, and the luminescence lifetime achieved 19.8 ns. The implanting of Janus nanometers particles into the white light-emitting diode devices greatly improved the stability of $CsPbX_3$ (X = Cl, Br, I) nanocrystals in air, water and light environments. However, the stability of these perovskite composites could be only manifested in the short term, and the external protection layers are not uniform and fine. It is well known that the surface passivation could eliminate the defects and dangling bonds and therefore increase their stability. In 2016, Huang et al. proposed a new and efficient surface passivation method, in which a stable mixed-halide passivation layer was formed on the surface of nanocomposites by ion exchange between $CsPbX_3$ (X = Br, I) perovskite nanocrystals and lead selenide

quantum dots. Results show that it not only improved the fluorescence quantum yield, but also significantly increased the photoelectric conversion efficiency and air stability of perovskite solar cells [17]. Coincidentally, Dalal et al. firstly demonstrated that some p-type semiconductors could be used as high-efficient perovskite-defective passivation materials, and a passivation mechanism was proposed [18]. Although some new p-type semiconductor showed excellent perovskite depletion passivation effect, the exploration of those good stability passivation agent would be the focal point in the future. It could imagine that if we combining wider band-gap semiconductor materials with perovskite nanostructures and forming an external protective layer around the $CsPbX_3$ (X = Cl, Br, I), the more stable and efficient $CsPbX_3$ nanostructures could be expected to manufacture.

In our previous work, we prepared $CsPbX_3$ (X = Cl, Br, I) perovskite nanocrystals by the hot-injection method and studied their optical properties [19, 20]. By varying the amount of PbX_2 (X = Cl, Br, I), the prepared $CsPbX_3$ nanocrystals possess high photoluminescence quantum yield (PLQY, about 70%), narrow full width at half-maximum (FWHM) (4–17 nm), tunable band gap (407–680 nm), and highly strong photostability. In this paper, we coated titanium precursor on the outside of the colloidal $CsPbBr_3$ NCs at room temperature and formed perovskite $CsPbBr_3$/TiO_2 nanocomposites with high dispersion and high crystallinity. By forming a $CsPbBr_3$/TiO_2 nanocomposite, we are trying to improve its PLQY and thermal stability. The optical mechanism, containing microstructure, chemical state and time-resolved decay process, was comprehensively studied.

2 Experimental section

2.1 Synthesis of $CsPbBr_3$/TiO_2 nanocrystals

The preparation process of $CsPbBr_3$ has been introduced in our previous papers [19, 20]. To synthesize the $CsPbBr_3$/TiO_2 nanocrystals, 15 μL TBOT with 1 mL toluene was added into a 250-mL 3-neck flask containing 20 mL of $CsPbBr_3$ nanocrystal solution under stirring. The solution was placed in a glove box with 30% relative humidity (RH) at room temperature for hydrolysis. After stirring for 3 h, the crude solution was centrifuged at 6,500 rpm for 8 min, and the precipitate was dried in Ar atmosphere at 300 °C for 2 h to obtain $CsPbBr_3$/TiO_2 core/shell NCs.

2.2 Characterization

In the experiments, X-ray diffraction (XRD), X-ray photoelectron spectroscopy (XPS), FT-IR spectrometer (FTIR), micro-Raman Spectroscopy (Raman) and high-resolution transmission electron microscopy (HRTEM) were carried

out for microstructural characterization of the obtained samples. The absorption properties were conducted on a double UV–Vis absorption spectrophotometer model 727. Room-temperature photoluminescence (PL) spectra were taken on an Edinburgh (FLS920) fluorescence spectrophotometer.

3 Results and discussion

Figure 1 shows X-ray diffraction patterns of the as-prepared $CsPbBr_3$ and $CsPbBr_3/TiO_2$ nanocrystals. It can be seen that the diffraction peaks of $CsPbBr_3$ NCs are consistent with the standard data file (JCPDS No. 54–0752), which confirms the accuracy of the cubic phase [21]. Two samples exhibit eight obvious peaks at 15.27°, 21.58°, 26.50°, 30.55°, 34.44°, 37.67°, 43.86° and 46.71°, corresponding to (100), (110), (111), (200), (210), (211), (220) and (300) planes, respectively. For $CsPbBr_3/TiO_2$ NCs, two additional diffraction peaks at ~ 23.8° and ~ 46.5° can be observed, which are assigned to (101) and (200) planes for anatase TiO_2 (JCPDS No. 89-4921) [22]. Simultaneous appearance of characteristic peaks for TiO_2 and $CsPbBr_3$ nanocrystals represents that the TiO_2 has successfully deposited on the surface of $CsPbBr_3$ NCs. Compared with $CsPbBr_3$ and TiO_2 nanocrystals, $CsPbBr_3/TiO_2$ NCs exhibits two additional diffraction peaks at 41° and 56.5°, which may originate from the residue or incomplete existence of TiO_2 shell.

Figure 2 shows HRTEM images of the monodisperse $CsPbBr_3/TiO_2$ NCs. From Fig. 2a, it can be seen that cube-shaped $CsPbBr_3$ NCs arranged neatly in nonpolar solvent and exhibited a high degree of crystallinity and stability. The average size is about 8.8 nm. From Fig. 2b, c, one can see that the plurality of $CsPbBr_3$ NCs is wrapped by one core−shell TiO_2 structure, which caused by the incomplete hydrolysis of high-concentration TBOT on the surface of $CsPbBr_3$ NCs. Figure 2d is the lattice fringe pattern of $CsPbBr_3/TiO_2$ nanocomposites, which reflects the
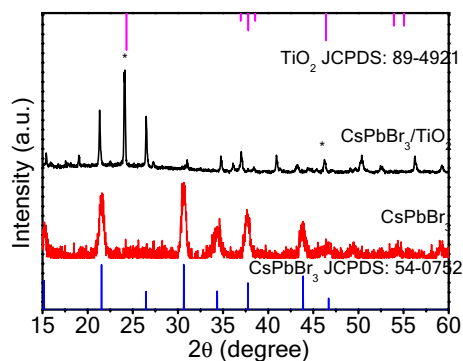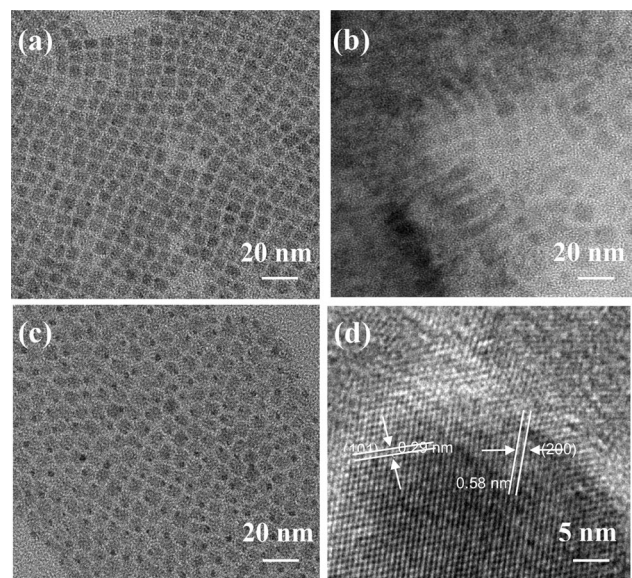

Fig. 2 HRTEM images of samples **a** $CsPbBr_3$ NCs, **b**, **c**, **d** $CsPbBr_3/TiO_2$ NCs
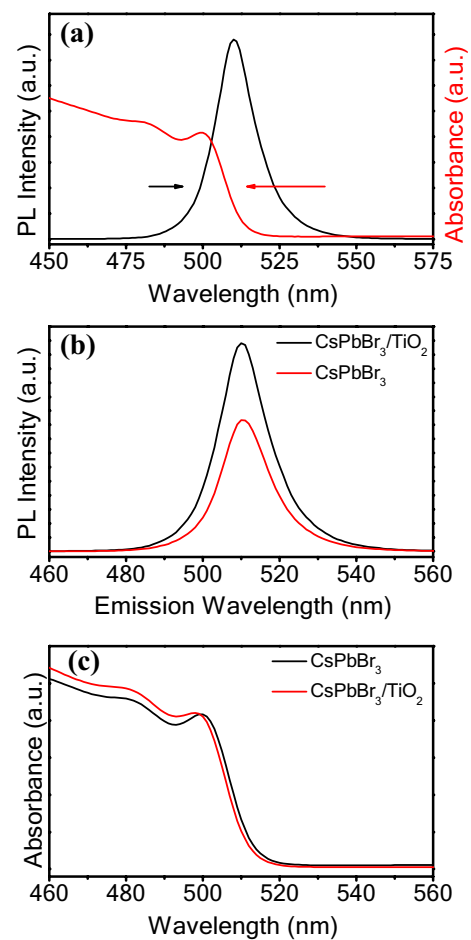

Fig. 3 a PL spectra and optical absorption spectra of $CsPbBr_3/TiO_2$ nanocomposites. **b** PL spectra of $CsPbBr_3$ and $CsPbBr_3/TiO_2$ NCs. **c** UV–visible absorption spectra of $CsPbBr_3$ and $CsPbBr_3/TiO_2$ NCs

**Fig. 1** XRD spectra acquired from $CsPbBr_3$ nanocrystals and $CsPbBr_3/TiO_2$ nanocomposites

0.58 nm lattice fringe of $CsPbBr_3$ NCs and 0.29 nm of TiO_2 NCs, corresponding to the (200) and (101) planes, respectively. More importantly, there is a clearance exist between $CsPbBr_3$ and TiO_2, meaning that a tight interface is formed between $CsPbBr_3$ and TiO_2.

To test the optoelectronic and electronic properties, the absorption and emission spectra of $CsPbBr_3$/TiO_2 nanocrystals were carried out, as shown in Fig. 3a. It exhibits an obvious slight of 9-nm Stokes shift between absorption edge and fluorescence peak, demonstrating the origin of direct band-gap bound exciton recombination, which could be attributed to the strong quantum confinement effect. After lasting in the air for one and two months, the photoluminescence and optical absorption spectra are measured to identify the stability of $CsPbBr_3$/TiO_2 nanocrystals, as shown in Fig. S1. Two patterns exhibit a similar small Stokes shift of 9 nm, showing high fluorescence and strong stability. Figure 3b shows the emission spectra of $CsPbBr_3$ and $CsPbBr_3$/TiO_2 NCs. Both of them show the analogous emission peak at about 510 nm, which demonstrate the similar size and uniform distribution, corresponding to the exhibition in Fig. 2. More precise observation reveals that the FWHM is about 15 nm, illustrating a favorable crystallinity and stability [23]. By

further comparison, it can be observed that there is an obvious increase in PL intensity of $CsPbBr_3$/TiO_2 nanocomposites. That means the as-prepared heterocomposites effectively inhibit the recombination of photogenerated charge carriers [24, 25]. From Fig. 3c, it can be seen that the absorption spectra of $CsPbBr_3$ NCs and $CsPbBr_3$/TiO_2 nanocomposites are broadcast. It can catch a strong sharp absorption peak at about 500 nm for $CsPbBr_3$ NCs and the absorption edge of the $CsPbBr_3$/TiO_2 nanocomposites blue-shifts to 498 nm for $CsPbBr_3$/TiO_2 NCs. In the range of 460 to 500 nm, the absorption capacity of $CsPbBr_3$/TiO_2 NCs is larger than that of $CsPbBr_3$, which is caused by the existence of amorphous TiO_2.

To explore the origin of emission for $CsPbBr_3$ and $CsPbBr_3$/TiO_2 nanocomposites, the PL and PLE spectra were carried out, as shown in Fig. 4. From the PLE spectra, as shown in Fig. 4a, a low-intensity broad peak at about 310 nm and a high-intensity broad peak at about 430 nm could be observed. Based on the PLE spectra, we measured the PL spectra under the center wavelength of 310 nm and 430 nm, as shown in Fig. 4b, c, respectively. Both of the two curves show a sharp peak at 508 nm, indicating that the emission at 508 nm is intrinsically linked with the excitation of 310 nm and 430 nm. To further research the

Fig. 4 **a** PLE spectra of $CsPbBr_3$ nanocrystals monitored at different wavelengths around 510 nm. **b** PL spectra of $CsPbBr_3$ nanocrystals taken under different excitation wavelengths around 310 nm. **c** PL spectra of $CsPbBr_3$ nanocrystals taken under different excitation wavelengths around 430 nm. **d** PLE spectra of $CsPbBr_3$/TiO_2 nanocrystals monitored at different wavelengths around 510 nm. **e** PL spectra of $CsPbBr_3$/TiO_2 nanocrystals taken under different excitation wavelengths around 430 nm
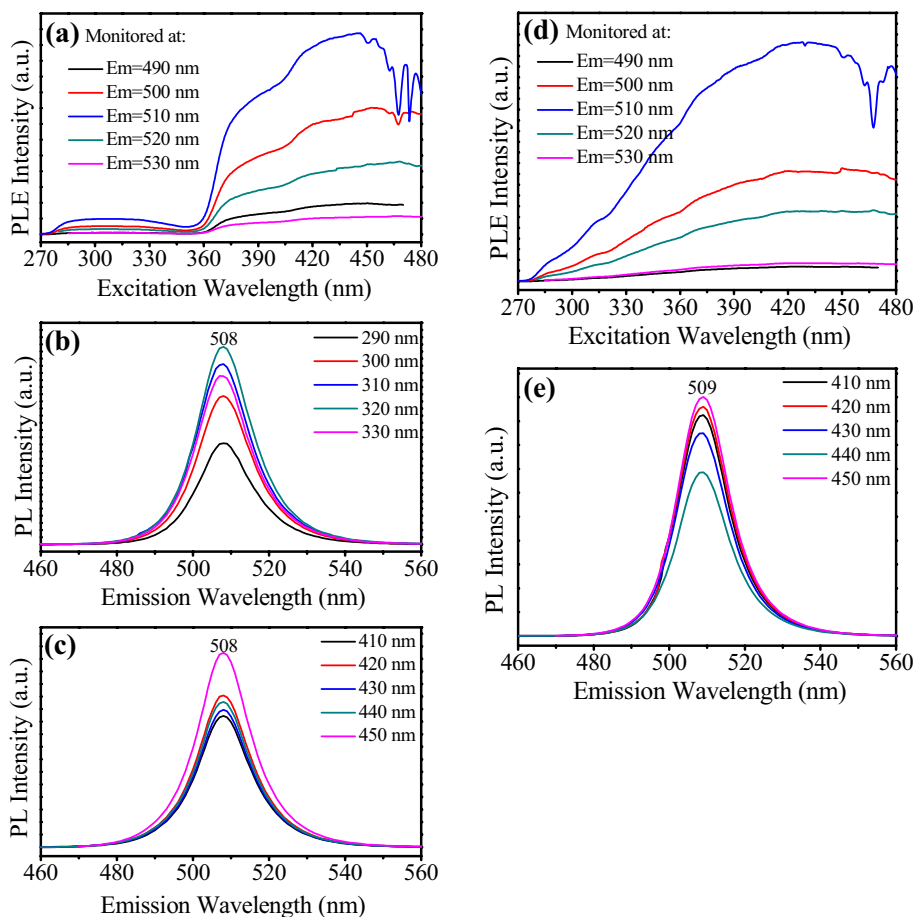
origins of emission of $CsPbBr_3/TiO_2$ nanocomposites, we also measured the PL and PLE spectra $CsPbBr_3/TiO_2$ at room temperature, as shown in Fig. 4d, e. It can be found that the PLE peak intensity increases with increasing the emission wavelength and reaches a maximum value when monitored at 510 nm. Additionally, the broad PLE band confirms that the perovskite nanocrystals can be excited under a broad wavelength. Compared with the PLE spectra of $CsPbBr_3$ and $CsPbBr_3/TiO_2$, they all show a peak at about 430 nm. However, the peak at 310 nm disappears for $CsPbBr_3/TiO_2$ nanocomposites, proving the successful compound of $CsPbBr_3$ with TiO_2. Combined with the above results, PL spectra of $CsPbBr_3/TiO_2$ nanocomposites under the excitation wavelength around 430 nm were implemented, as shown in Fig. 4e. One can see that all curves exhibit a sharp emission peak at 509 nm and do not shift with changing the excitation wavelengths, which exhibits the uniform size distribution of nanocrystals, matching the images in Fig. 2. With increasing the excitation wavelength, the PL intensity increases and shows the maximum value at 450 nm, illustrating that the emission at 509 nm is intrinsically linked with the excitation at 430 nm. The PLE spectra of $CsPbBr_3/TiO_2$ nanocrystals after lasting one and two months in the air by monitoring at 510 nm as center wavelength were carried out, as shown in Fig. S2 and Fig. S3. Both of them show a maximum absorption under monitoring at 510 nm, which exhibit the same behaviors with the original $CsPbBr_3/TiO_2$ nanocomposites. It is interesting that the curves measured after lasting in the air for a month present two saturation excitation peaks at 380 nm and 430 nm. The PLE curves show the fixed single emission peak at 508 nm, illustrating the excellent stability of $CsPbBr_3/TiO_2$ nanocrystals. Similarly, as shown in Fig. S3, the absorption peak shifts to 350 nm, which is caused by the surface passivation. The emission peak pinned at 508 nm, further demonstrating the excellent chemical stability and photostability of $CsPbBr_3/TiO_2$ nanocrystals.
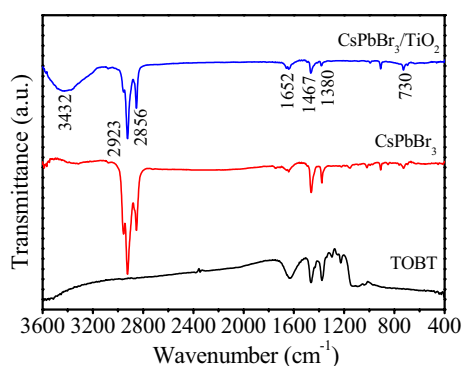
To explore the molecular structure and surface bonds of $CsPbBr_3/TiO_2$ nanocrystals, the FTIR spectroscopy for the samples was performed, as shown in Fig. 5. Compared with the $CsPbBr_3$ and $CsPbBr_3/TiO_2$ NCs, the decrease in two fundamental sharp peaks at 2923 and 2856 cm^{-1} suggests the loss of carbonaceous residues and dehydroxylation process. The decrease in another two peaks at 1468 and 1380 cm^{-1} indicates the losing of COO^- and $-CH_3$ groups. Besides, there is an increased intensity of surface-adsorbed water (H–O–H) at 3432 cm^{-1} and hydroxyl groups (O–H) at 1652 cm^{-1}, plus a slight increase at about 730 cm^{-1} for Ti–O–Ti bonds, stating the coating of titanium matrix on $CsPbBr_3$ nanocrystals.

To achieve the surface states and compositions of the samples, the X-ray photoelectron spectrum XPS is conducted, as presented in Fig. 6. Compared with the $CsPbBr_3$, two additional peaks of Ti and O are observed in $CsPbBr_3/TiO_2$ NCs, indicating a successfully forming of $CsPbBr_3/TiO_2$ nanocomposites. The lower intensity of $CsPbBr_3/TiO_2$ NCs is caused by the existence of TiO_2 shell. Figure S4 is the fine XPS of $CsPbBr_3/TiO_2$ NCs. From Fig. S4a, it can be seen that there are only Cs, Pb, Br, Ti, N and O elements in the sample and no other elements are detected, showing good purity of as-prepared samples. The Cs, Pb and Br elements are contributed by the perovskite nanocrystals, while the N and part of O elements are related to the chemical adsorption of OA and OAm ligands [26]. From Fig. S4b, one can see two rough symmetrical peaks at 738.2 and 724.3 eV, corresponding to Cs 3d 5/2 and Cs 3d 3/2, respectively. Figure S4c shows the spin–orbit splitting energy of 4.8 eV from two sharp peaks at 138.2 and 143.0 eV for Pb 4f 7/2 and Pb 4f 5/2, respectively, which are characteristic for Pb^{2+} in $CsPbBr_3/TiO_2$ nanocrystals. Similarly, in Fig. S4e, the strong peak at 458.6 eV matches with Ti 2p 1/2, while the low peak at 464.2 eV matches with Ti 2p 3/2, which confirms the Ti^{4+} valence. In particular, Fig. S4d shows one single broad peak and can be deconvoluted into two
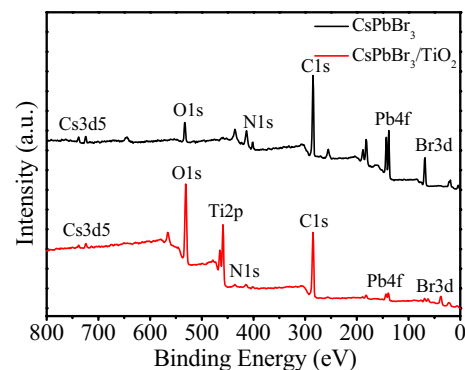

Fig. 5 FTIR absorption spectra of $CsPbBr_3$ nanocrystals and $CsPbBr_3/TiO_2$ nanocomposites

Fig. 6 XPS spectra of $CsPbBr_3$ nanocrystals and $CsPbBr_3/TiO_2$ nanocomposites
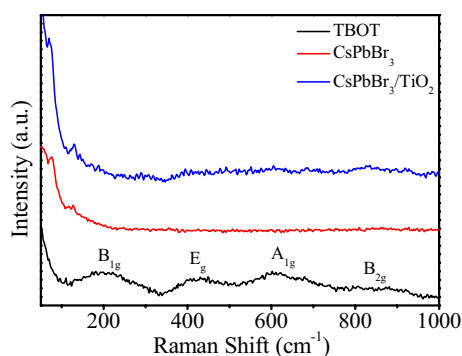
Fig. 7 Raman spectra acquired from TBOT, CsPbBr$_3$ and CsPbBr$_3$/TiO$_2$ nanocomposites
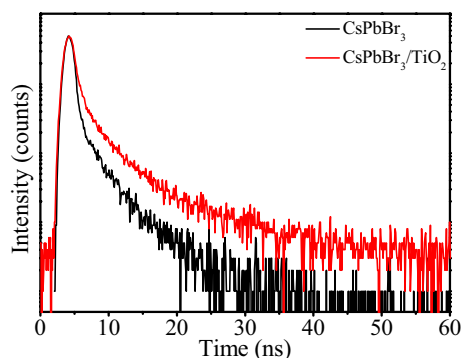

Fig. 8 Time-resolved PL decay curves obtained from CsPbBr$_3$ and CsPbBr$_3$/TiO$_2$ nanocomposites

subpeaks. The binding energy at 69.3 eV can be ascribed to the bromine in [PbBr$_6$]$^{4-}$ octahedron, and the peak at 68.3 eV can be ascribed to the bromine in CsPbBr$_3$/TiO$_2$ NCs. Figure S4f is the O1s meticulous scan spectrum, which could be deconvoluted into two subpeaks. The main separation peak at 531.9 eV corresponds to lattice oxygen in the hydroxyl groups and another minor separation peak at 529.9 eV corresponding to adsorption oxygen in the Ti–O of TiO$_2$. Figure S5 and Fig. S6 are the XPS of samples lasting in the air for one and two months. Compared with the original samples, the similar phenomenon of the element meticulous scan spectrogram except oxygen is presented. By analyzing the characteristic profiles in Fig. S5(f) and S6(f), one can see that the main separation peak related to O–H functional groups decreases with lasing in the air, which is caused by the loss of hydroxyl groups for the dehydration with the time.

Raman spectroscopy is a powerful technique to identify the molecular structure of perovskite nanocrystals. Figure 7 shows the Raman spectrum of TOBT, CsPbBr$_3$ and CsPbBr$_3$/TiO$_2$ NCs. From the figure, we can see that CsPbBr$_3$/TiO$_2$ NCs contain two sharp peaks in CsPbBr$_3$ NCs and four weak peaks in TOBT armamentarium. The

peaks at about 70 and 120 cm^{-1} are ascribed to the vibrational mode of [PbX$_6$]$^{4-}$ octahedron and motion of Cs$^+$ cations, respectively [27]. The peaks at about 175, 420 and 620 cm^{-1} are ascribed to the stress change of O–Ti–O variable angle vibration. Both of them indicate the formation of TiO$_2$ core/shell with an anatase-like structure.

Figure 8 and S7 reveals the time-resolved photoluminescence decay spectrum for CsPbBr$_3$ and CsPbBr$_3$/TiO$_2$ nanocomposites. A radiative emission decay with about 4.04 ns average lifetime of CsPbBr$_3$/TiO$_2$ NCs can be obtained. However, the radiative emission decay time of CsPbBr$_3$ NCs is about 2.52 ns, indicating that the energy transfer happens between CsPbBr$_3$ and TiO$_2$. After lasting months in the air, the lifetime of CsPbBr$_3$/TiO$_2$ NCs keeps at about 3.98 ns and 3.81 ns, meaning the high stability of perovskite nanocomposites after coating with the TiO$_2$. Deposition of TiO$_2$ shell reduces the surface defects of nanocrystals and increases the non-radiative transitions, thereby improving the lifetimes of CsPbBr$_3$/TiO$_2$ nanocrystals. The defect tolerance of CsPbBr$_3$ NCs offers a long lifetime and high PLQY, causing improved stability for CsPbBr$_3$/TiO$_2$ perovskite nanocomposites.

To further check the thermal stability of perovskite nanostructures, we tested CsPbBr$_3$/TiO$_2$ nanocrystals annealing at 80 °C, as shown in Fig. S8-S11. The XRD characteristic diffraction peaks after annealing were similar to the original sample, illustrating the stability of CsPbBr$_3$. In Fig. S9, there was a Stokes shift of 10 nm, demonstrating the emission originated from the exciton recombination. Figure S10 is the fluorescence spectroscopy of CsPbBr$_3$/TiO$_2$ NCs under different excitation wavelengths. One could see an excitation peak at about 400 nm and an emission peak at about 508 nm in PLE and PL spectra. Unchanged emission peaks present the uniform size distribution of nanocrystals and robust stability of the sample after annealing. Figure S11 is the time-resolved PL decay curves of CsPbBr$_3$/TiO$_2$ nanocrystals before and after post-annealing. The PL decaying time of about 3.13 ns indicates a high thermal stability of perovskite nanocrystals.

4 Conclusions

In summary, we successfully prepared monodispersed colloidal CsPbBr$_3$/TiO$_2$ core/shell nanocomposite. The CsPbBr$_3$/TiO$_2$ nanocomposite exhibits a uniform size distribution of about 9.2 nm. A narrow FWHM indicates good crystallinity and favorable stability. The time-resolved photoluminescence decay lifetime of CsPbBr$_3$/TiO$_2$ nanocrystals increases to 4.04 ns which that of CsPbBr$_3$ is 2.52 ns, which leads to a high PLQY. After a

post-annealing at 80 °C, it was found that the emission peak and fluorescence lifetime of $CsPbBr_3/TiO_2$ nanocrystals remained unchanged, indicating the prepared composite nanocrystals have a strong thermal stability. The results provide an effective method to improve the stability of perovskite nanostructures and are expected to have a practical application in optoelectronic fields.

Declarations

Conflict of interest The authors declare that they have no conflict of interest.

References

1. Wang X et al (2018) High-quality in-plane aligned $CsPbX_3$ perovskite nanowire lasers with composition-dependent strong exciton-photon coupling. ACS Nano 12(6):6170–6178

2. Liu TJ et al (2020) High charge carrier mobility in solution processed one-dimensional lead halide perovskite single crystals and their application as photodetectors. Nanoscale 12(17):9688–9695

3. Wang Y et al (2018) White LED based on CsPbBr3 nanocrystal phosphors via a facile two-step solution synthesis route. Mater Res Bull 104:48–52

4. Ji L et al (2020) Large organic cation incorporation induces vertical orientation growth of Sn-based perovskites for high efficiency solar cells. Chem Eng J 402:125133

5. Kojima A et al (2009) organometal halide perovskites as visible-light sensitizers for photovoltaic cells. J Am Chem Soc 131(17):6050–6051

6. Pistor P et al (2018) Thermal stability and miscibility of co-evaporated methyl ammonium lead halide ($MAPbX_3$, X=I, Br, Cl) thin films analysed by in situ X-ray diffraction. J Mater Chem A 6(24):11496–11506

7. Liu P et al (2017) Organic–inorganic hybrid perovskite nanowire laser arrays. ACS Nano 11(6):5766–5773

8. Green MA et al (2015) Solar cell efficiency tables (Version 45). Prog Photovolt 23(1):1–9

9. Liu Y et al (2016) Thinness- and shape-controlled growth for ultrathin single-crystalline perovskite wafers for mass production of superior photoelectronic devices. Adv Mater 28(41):9204–9209

10. Bian H et al (2018) Graded bandgap CsPbI2+xBr 1–x perovskite solar cells with a stabilized efficiency of 14.4%. Joule 2(8):1–11

11. Chen Q et al (2020) Co-solvent controllable engineering of $MA_{0.5}Pb_{0.8}Sn_{0.2}I_3$ lead-tin mixed perovskites for inverted perovskite solar cells with improved stability. Energies 13(10):2438

12. Shan Q et al (2017) All-inorganic quantum-dot light-emitting diodes based on perovskite emitters with low turn-on voltage and high humidity stability. J Mater Chem C 5(18):4565–4570

13. Hu H et al (2018) Interfacial synthesis of highly stable $CsPbX_3$/oxide janus nanoparticles. J Am Chem Soc 140(1):406–412

14. Wang HC et al (2016) Mesoporous silica particles Integrated with All-inorganic CsPbBr3 perovskite quantum-dot nanocomposites (MP-PQDs) with high stability and wide color gamut used for backlight display. Angew Chem Int Ed 55(28):7924–7929

15. Chen W et al (2017) Enhanced stability and tunable photoluminescence in perovskite $CsPbX_3$/ZnS quantum dot heterostructure. Small 13(21):1604085

16. Zhang Z et al (2017) A new passivation route leading to over 8% efficient PbSe quantum-dot solar cells via direct ion exchange with perovskite nanocrystals. Adv Mater 29(41):3214–3321

17. Ye S et al (2017) A breakthrough efficiency of 19.9% obtained in inverted perovskite solar cells by using an efficient trap state passivator Cu(thiourea)I. J Am Chem Soc 139(22):7504–7512

18. Abbas HA et al (2015) High efficiency sequentially vapor grown n-i-p $CH_3NH_3PbI_3$ perovskite solar cells with undoped P3HT as p-type heterojunction layer. APL Mater 3:016105

19. Chen HT et al (2019) Tunable photoluminescence of CsPbBr3 perovskite quantum dots for their physical research. Appl Suf Sci 465:656–664

20. Chen HT et al (2019) Highly luminescent $CsPbX_3$ (X=Cl, Br, I) perovskite nanocrystals with tunable photoluminescence properties. J Alloys Compd 789:392–399

21. Gao L et al (2017) Passivation of defect states in anatase TiO_2 hollow spheres with Mg doping: realizing efficient photocatalytic overall water splitting. Appl Catal B 202:127–133

22. Kim Y et al (2015) Efficient luminescence from perovskite quantum dot solids. ACS Appl Mater Interfaces 7(45):25007–25013

23. Li C et al (2017) Enhanced photoresponse of self-powered perovskite photodetector based on ZnO nanoparticles decorated CsPbBr3 films. Sol Energy Mater 172:341–346

24. Liu X et al (2018) Enhanced X-ray photon response in solution-synthesized CsPbBr3 nanoparticles wrapped by reduced graphene oxide. Sol Energy Mater 187:249–254

25. Chen H et al (2011) Defect-related energy structures of aln nanotips probed by photoluminescence. J Phys D Appl Phys 44(50):505304

26. Xia H et al (2018) High binding ability ligand controlled formation of $CsPbX_3$ (X = Cl/Br, Br, I) perovskite nanocrystals with high quantum yields and enhanced stability. RSC Adv 8(63):35973–35980

27. Chen D et al (2018) $CsPbX_3$ (X= Br, I) perovskite quantum dots embedded low-melting phosphosilicate glasses: controllable crystallization, thermal stability and tunable emissions. J Mater Chem C 6(25):6832–6839

Publisher's Note Springer Nature remains neutral with regard to jurisdictional claims in published maps and institutional affiliations.